ACS OMEGA

http://pubs.acs.org/journal/acsodf

Article

Oxygen Scavenging Hybrid Nanostructure: Localization of Different Iron Nanoparticles on Montmorillonite Clays Host

Khadijeh Khederlou,* Reza Bagheri, Akbar Shojaei, Nathalie Gontard, and Yousef Tamsilian

Cite This: *ACS Omega* 2022, 7, 16391−16401

Read Online

ACCESS | Metrics & More | Article Recommendations

ABSTRACT: According to the great potential of zero-valent iron nanoparticle applications in the environmental, medical, chemical, packaging and many other industries, there is still a need to tailor their production methods. This study reports the production of a hybrid nanostructure based on iron nanoparticles (INPs) produced in/on montmorillonite (MMT) nanoclays as an oxygen scavenger and barrier additive in polymeric packaging materials of oxygen-sensitive products. INPs and MMT were demonstrated to have effective mutual interactions in which the MMT host played a chemophysical trapping role for iron particles, causing smaller particles around 10 nm with 6.2 g/m^2 higher specific surface area by limiting particle growth and agglomeration. In return, the embedding of primary iron cations in/on clays and growth of these particles during the reduction reaction pushed the clay layers out and helped further clay intercalation−exfoliation. Effective study of solvent and primary cation (Fe^{2+}/Fe^{3+}) types showed different preferences in interacting with natural and alkylammonium-modified MMT, resulting in the different site selection. Fe^{2+} cations preferred to migrate to the interlayer space, whereas Fe^{3+} cations tended to bond to the clay surface. The obtained results in this study suggest tailoring the ultimate oxygen scavenging capacity, shelf life, and migration properties of a hybrid nanoparticle according to the application requirements.

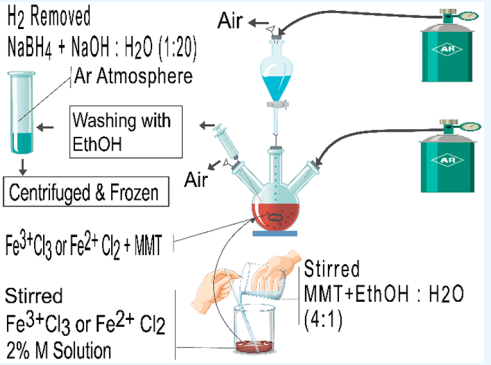

1. INTRODUCTION

Highly reactive zero-valent iron nanoparticles (ZVINPs) are some of the most important synthetic nanoparticles due to their high specific surface area, strong reducing power, and biocompatible properties which enable them to have many potential applications such as environmental (e.g., soil remediation, groundwater decontamination, water purification),[1−10] biomedical (e.g., imaging or targeted anticancer therapy),[11−13] and food contact materials (e.g., active and intelligent packaging).[14,15] Researchers report excellent uptake capabilities, less pollution, and more availability toward various types of metallic ions for ZVINPs.[16,17]

These reactive materials have been applied in permeable reactive barriers for the removal of different pollutants,[18−21] bacteria,[22,23] and oxygen and other scavenging components.[24,25] In the latter case, some rapidly emerging prominent technologies with considerable potential benefits of ZVINPs have been developed because the most commercially available and heat-stable oxygen scavengers are sachet form.[26]

The potential risks of sachets for consumer misuse, ingestion, and leakage contaminate the products, and the requirement of a high oxygen absorption rate to prevent initiation of oxidation mechanisms for the food degradation supports the idea of an oxygen absorption system in which to imbed polymeric materials.[15,27]

Iron nanoparticles with an average diameter of 110 nm have been studied as oxygen scavengers to prevent lipid oxidation of roasted sunflower seeds and walnuts. The scavenger capacity was almost 10 times greater than that of conventional iron powders.[14] On the nanoscale, the specific surface area of iron particles is 30 times more than micron size.[28,29] Most of the reported ZVINP sizes produced by different research groups are 100−200 nm,[19−21,29−32] and just a few groups reported the ZVINP were produced in a size below 30 nm.[1,33−35]

Over the years, the classic borohydride reduction method for preparing ZVINPs has been modified using various stabilizers or surface modifiers to acquire more stable and appropriate ZVINP delivery for scavenging gaseous oxygen, treating different organic and inorganic contaminants in water and soil,[4,36,37] and targeting drug delivery and improved magnetic resonance imaging.[38]

Reducing an aqueous iron salt in the presence of a support material can reduce the effect of iron nanoparticle aggregation,

Received: January 14, 2022
Accepted: April 13, 2022
Published: May 4, 2022

Table 1. Formulation of Prepared INP-Imbedded MMT Clay and Zero-Valent Iron Nanoparticle Samples

		INP-imbedded MMT clay				ZVINPs	
solution	compound	Fe03−C20A	Fe02−C20A	Fe03−CNa^+	Fe02-CNa^+	Fe03	Fe02
clay−salt dispersion	C20A	3 g	3 g				
	CNa^+			3 g	3 g		
	$FeCl_3·6H_2O$	2.420 g, 0.2 M (0.5 g Fe)		2.420 g, 0.2 M (0.5 g Fe)		2.420 g, 0.2 M (0.5 g Fe)	
	$FeCl_2·4H_2O$		1.781 g, 0.2 M (0.5 g Fe)		1.781 g, 0.2 M (0.5 g Fe)		1.781 g, 0.2 M (0.5 g Fe)
	H_2O	8.9 g	8.9 g	8.9 g	8.9 g	8.9 g	8.9 g
	C_2H_5OH	35.8 g	35.8 g	35.8 g	35.8 g	35.8 g	35.8 g
	$NaBH_4$	0.677 g	0.677 g	0.677 g	0.677 g	0.677 g	0.677 g
reducing agent	H_2O	44.7 g	44.7 g	44.7 g	44.7 g	44.7 g	44.7 g
	NaOH	2.23 g	2.23 g	2.23 g	2.23 g	2.23 g	2.23 g

offering a higher specific surface area and consequently a higher reactivity.[19,28,39]

A number of researchers have attempted to anchor iron nanoparticles on solid supports such as zeolites,[40−43] graphene and active carbons,[10,12,44,45] and nanoclays.[46−52] This strategy provides several advantages like surpassing the aggregation of zero-valent iron nanoparticles and protecting particles from the oxidation to more easily disperse in a polymer matrix for further applications.

In recent years, among all potential supports, nanoclays have attracted considerable interest as an iron particle support due to their high specific surface area and unusual intercalation properties. Eliminating microbes, anions, and hazardous compounds,[1,53,54] immobilizing the enzymes,[5] and preparing conductive nanocomposites[55] are some productive targets of utilizing iron−clay combinations. Most of these studies have used kaolinite or bentonite support.[5,46,56] Few studies are available related to producing iron nanoparticles using borohydride solution reduction in the presence of the MMT host, in which the mean size of produced INPs is more than 50 nm.[46,57]

Despite the similar initial *d* value of clay platelets in kaolinite and MMT, the surface charge and cation exchange capacity (CEC) in kaolinite ($3−15 \times 10^{-5}$ equiv/g) is much lower than that of MMT ($80−100 \times 10^{-5}$ equiv/g).[58] This small ion exchange capacity initiated from H-bonding interlayer forces makes it difficult to seek good results to increase the *d* value between platelets modified by alkylammonium ion. Hence, kaolinite has poor dispersion results in hydrophobic matrixes.[59]

On the other hand, normally, the specific surface area of kaolinite is less than MMT depending on the ordering of these clays.[49] MMT is a naturally 2:1-type layered aluminosilicate with a turbostratic structure,[60] where each layer comprises an alumina octahedral sheet sandwiched between two silicate tetrahedral sheets, and the layer has a permanent negative charge resulting from isomorphous substitution occurring mainly in the octahedral sheet. Such layers are stacked by weak dipolar or van der Waals forces, leading to the intercalation of charge-compensating cations into the interlayer space and causing MMT to be easily expanded along the *c*-direction. Therefore, not only adsorption of target components on the external surface but also introduction of these components into the interlayer space can occur.[46]

Surveying advantages of MMT and embedding INP in the polymeric materials for the oxygen scavenging system, the main purpose of this work is to explore new pathways of INP production and to develop additional knowledge to modulate INP reactivity for optimizing the oxygen scavenging capability of iron-based active systems in food packaging materials. The ultimate objective is to investigate INP preparation conditions and to clarify the position of INP produced from different iron cations (Fe^{2+}/Fe^{3+}) located on MMT supports.

2. EXPERIMENTAL SECTION

2.1. Materials. Natural montmorillonite (CNa^+), organically modified montmorillonite with dimethyl dehydrogenated tallow and quaternary ammonium (C20A), was supplied by Southern Clay Products Inc. (Texas, USA). Two different iron salts, $FeCl_2·4H_2O$ and $FeCl_3·6H_2O$, sodium borohydride ($NaBH_4$, 99%), ethanol (C_2H_5OH, EtOH, 99.8%), and sodium hydroxide solution (NaOH, 97%) were obtained from Sigma-Aldrich (France).

2.2. Preparation of Compounds. ZVINP and INP-MMT particles were produced by some new modifications on Wang and Zhang's method.[29] Table 1 shows the formulation of prepared samples. According to the CEC of 100×10^{-5} equiv/g for C20A, at least 100 g of MMT has the absorbing capacity of 2.8 g of Fe^{2+} by Fe/clay 1:36 and 1.9 g Fe^{3+} by Fe/clay 1:54 in the interlayer space. Considering the Fe absorption on the surface and edges, it was found that this ratio should be as large as 1:6 for the effective oxygen absorption.

In all samples, the clay (C20A or CNa^+) was dispersed in an ethanol/deionized water solution (4:1 V/V) and then added to the 0.2 M solution of iron salt ($FeCl_2·4H_2O$ or $FeCl_3·6H_2O$) with stirring for 40 h. The reducing agent solution was prepared by stirring 0.4 M of $NaBH_4$ in water/NaOH (32%) (20:1) and H_2 removal by degassing for 20 h. Both clay−salt and reducing agent solution volume were 100 mL.

The clay−salt dispersion was transferred and stirred into a sealed three-neck flask under argon gas purging by two syringe needles for 30 min. Meanwhile, the reducing agent was transferred to a sealed flask and Ar purged in the same way. The two flasks were connected by a sealed pipe continuously with a syringe needle. The reducing agent was added at ra ate of 2−3 droplets/min to the dispersion under stirring (400 rpm), and the produced H_2 was continuously purged with a syringe needle. The final dark solution was stirred for 20 min after the reaction was finished.

Sixty milliliters of the produced solution was placed into centrifuge cells capped by elastic stoppers and filled with Ar gas and centrifuged for 3 min at a speed of 4000 rpm. The resultant particles were washed and centrifuged three times with absolute ethanol and poured into several cells filled with Ar gas and frozen at −40 °C for 1 h. Finally, the powders were obtained with a

https://doi.org/10.1021/acsomega.2c00286
ACS Omega 2022, 7, 16391−16401

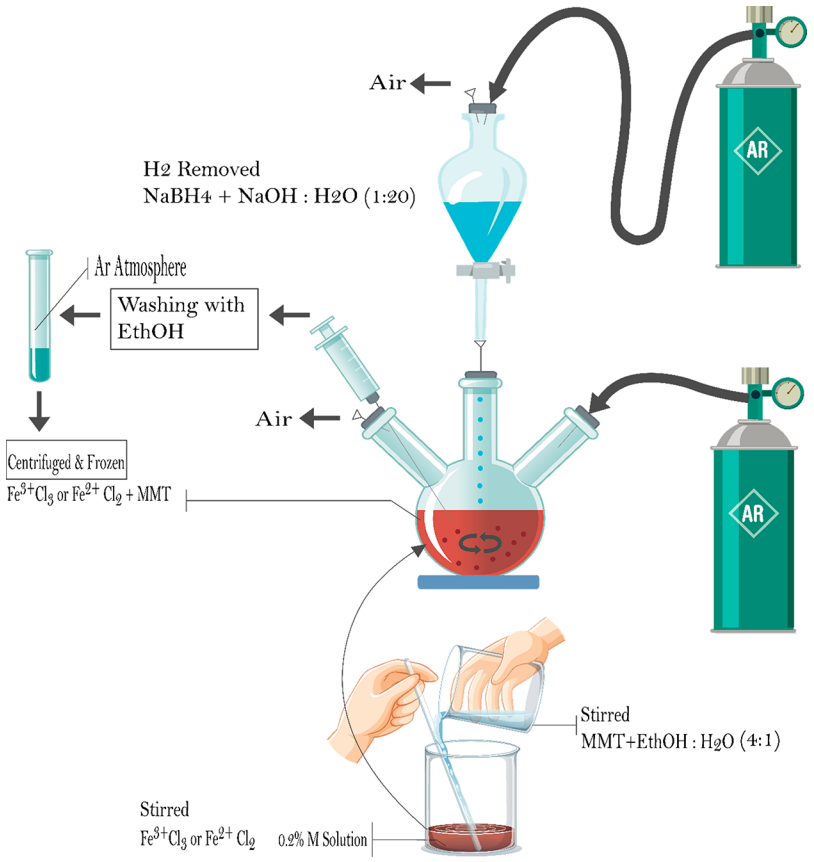

Figure 1. Production procedure schematic of the iron nanoparticle embedded in the MMT clay.

freeze-dryer (Christ Alpha 2-4 LSC, Osterode, Germany) at −100 °C and 0.3 mbar overnight. To compare, Fe^0 (ZVINPs), was produced from Fe^{2+} and Fe^{3+} cations with the same process in the absence of clay. Considering that the surface charge of CNa^+ originated from OH groups and the polarity of C20A, it was hypothesized that polar solvent having OH groups such as ethanol could facilitate the clay dispersion compared to conventionally used aqueous solution. The ethanol/water ratio of 4:1 (v/v) was selected as the dispersing solvent, having enough water for the Fe cations for the reduction reaction to ZVINPs. Moreover, as the hydrogen ions were responsible for the ZVINP resolubilization, a small amount of sodium hydroxide, NaOH, was added to the borohydride reducing solution to neutralize H^+ ions. Figure 1 shows the production procedure schematic of the iron nanoparticle embedded in the MMT clay.

2.3. Characterization and Measurement. X-ray diffraction (XRD) patterns from samples were obtained using a PANalytical X'Pert diffractometer (Malvern Panalytical Ltd., Malvern, UK) with Cu Kα radiation (λ = 1.54 Å) in the reflection mode.

The average diameter size of the resulting INPs was approximated from the XRD spectra using the Scherer equation as follows:[61]

$$L = \frac{K \cdot \lambda}{(\beta_{obs} - \beta_{instrm}) \cdot \cos(\theta)} \quad (1)$$

In this equation, L is particle size (nm), λ is the radiation wavelength (nm), K is Scherer constant (0.94, usually $0.87 < K < 1$), β_{obs} is the observed full width at half-maximum intensity (rad), and β_{insrm} is instrumental broadening (rad) as a function of 2θ. The XRD experiments were repeated to check the reproducibility of the results. The repeated experiments showed that the experimental errors were in the range of ±1−1.5% INP diameters.

Transmission electron microscopy (TEM) images were taken from the powder suspensions with a Hitachi H7100 (St George's, University of London, UK) motorized and digitized stage, high-resolution (0.4 nm) and high-contrast (25 to 125 kV) microscope equipped with a 1024 × 1024 pixel digital camera. For the sample preparation, all samples were dropped on carbon foam wafers, and the residual solvent was removed with filter paper.

Specific surface area (SSA) of the samples was measured by N_2 gas adsorption according to the Brunauer−Emmett−Teller (BET) method equipped with a Micromeritics ASAP 2460 surface area and porosity analyzer (Micromeritics Instrument Corp., Norcross, USA). The degassing process was done by heating the samples in vacuum at the temperature of 50 °C and for 48 h. For a better understanding of the preferred adsorption sites in/on the clay platelets for Fe cations before the reduction, the calculated SSA from BET isotherms was compared. Experimental errors were in the range of ±0.2% SSA.

$$\text{calculated SSA} = \sum \text{wt \%} \times \text{SSA (from BET isotherms)} \quad (2)$$

Cryogenic Mossbauer spectroscopy of the samples was obtained by a constant-acceleration-type Mossbauer spectrometer incorporating either a microprocessor or an Ortec model 6200 multichannel analyzer with 1024 channels operating in the multiscale mode for the data storage. The γ-ray source was ^{57}Co in Pd of 50 mCu (1.85 × 109 Bq) nominal strength, and an

https://doi.org/10.1021/acsomega.2c00286
ACS Omega 2022, 7, 16391−16401

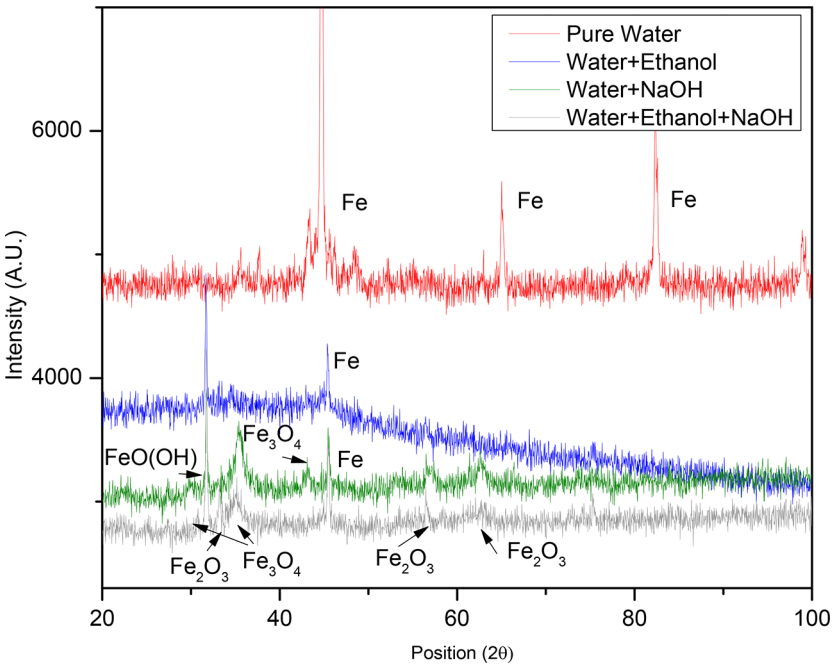

Figure 2. XRD spectra of Fe03 ZVINPs produced in various solvents (water + EtOH + NaOH for the salt solution and water + NaOH for the reducing agent).

argon/methane proportional counter was used as the γ-ray detector.

Oxidation extent and color change of the samples by consuming the ambient oxygen during the time were measured using a colorimeter.

3. RESULTS AND DISCUSSION

Solvent type, iron cation valent, and chemophysics of the MMT layered structures were categorized as parameters affecting the INP particle size and morphology. Cation and clay types as INPs controlling parameters are also studied.

3.1. Solvent Effect. Figure 2 shows the XRD spectra of the INPs produced with various solvents for the dispersing and/or reducing solutions. The average diameters of the ZVINPs approximated from the XRD spectra are presented in Table 2 for the different solvents.

Table 2. Average Fe03 ZVINP Diameter Produced in Various Solvents

solvent	particle diameter (nm)
water	82
water + ethanol	67
water + NaOH	40
water + ethanol + NaOH	65

According to Figure 2, adding EtOH and NaOH to the dispersing and reducing agent solutions, respectively, herein after the solvent for the mixed three is selected, could enhance the probability of Fe oxides and Fe hydroxide production. This could be due to the increasing O_2 solubility of more than 5 times compared to that of pure water and the presence of OH groups in the solution.[62,63]

On the other hand, Table 2 shows that the presence of EtOH and NaOH in water decreased the average particle diameter compared to pure water. According to the results of previous studies,[64,65] this phenomenon could be due to the hydrogen bonding of EtOH and NaOH with Fe_3O_4 (magnetite) and FeO (wustite) surfaces during the reduction reaction. These were reported as intermediate states before becoming fully reduced iron[64,66] to retard the INP growth and its great tendency toward agglomeration because of steric effects coming from van der Waals forces.[65]

3.2. Cation Type Effect. Fe^{2+} and Fe^{3+} have different ion diameters and chemical characteristics, and therefore their reduction products are expected to have further different interactions with MMT. Figure 3 shows XRD spectra of the ZVINPs produced from different cations.

The resulting particle size was calculated to be 65 and 73 nm for Fe^{3+} and Fe^{2+} cations, respectively. As illustrated in the reflection intensities of Figure 3, using Fe^{2+} decreased Fe_2O_3 in the solution by increasing FeO as the precursor of Fe_2O_3 and Fe_3O_4 production accelerated. Producing more Fe_3O_4 made bigger particles. This was in good agreement with the previous findings to illustrate the effect of increasing Fe^{2+}/Fe^{3+} ratio in producing bigger iron oxides, as suggested by Glavee et al.[63] and Yan and Zhang.[66]

3.3. Clay Host Effect. The TEM images of the Fe^{3+} nanoparticles produced alone and in the presence of C20A MMT are shown in Figure 4. As shown in Figure 4a, the produced particles tended to form large aggregates, which could adversely affect their scavenging performance.[50]

According to Figure 4b,c, the growth of INPs produced from Fe^{3+} cation in/on C20A clay platelets and in the selected solvents reduced the average particle diameter from 50 to 10 nm, which is being reported for the first time. The existing OH groups in MMT on the sheets and edges led to more cations being adsorbed as seeds of final INPs and resulted in smaller particles according to the growth kinetics.[67] In addition to the trapping role of chemical groups of the clay surface and edges, the limited interlayer space of MMT could act as a cage for the Fe cations and limited the INP growth during the reduction process. On the other hand, Figure 4b,c shows that the INP growth on and between the clays dispersed the MMT platelets to

https://doi.org/10.1021/acsomega.2c00286
ACS Omega 2022, 7, 16391−16401

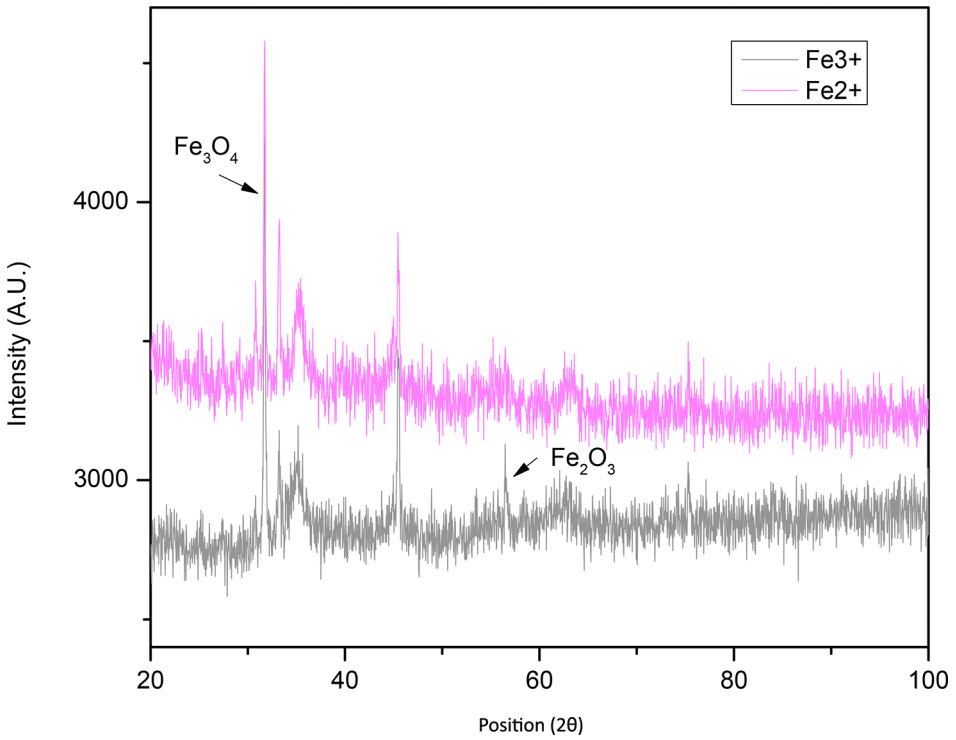

Figure 3. XRD spectra of Fe02 and Fe03 ZVINPs produced in selected solvent.

support the oxygen scavenging. Kombaya-Touckia-Linin et al. showed that this INP has a capacity 4 times more than that of an α-tocopherol-based system.[68]

As illustrated in Figure 4d, removing the selected solvent INPs appeared to agglomerate in MMT edges. As removing the solvent will cause the strong H-bonding of solvent reduction products (INPs and its oxides) to disappear, these products tended to agglomerate by weak van der Waals forces and interacted with OH groups on the MMT surface and edges.

Figure 5 shows a schematic view of the clay surface effect on the Fe cation reduction.

3.4. Particle Localization. The calculated and measured SSA from BET isotherms is presented in Table 3 to show the particle localization in/on the clay platelets for Fe cations before the reduction.

According to Table 3, adding alkylammonium ions to C20 compared to adding to CNa^+, despite of increasing the d value, decreased the SSA from 47.00 to 9.33 g/m^2 by the steric effect of alkyl chains. Alkylammonium tallow occupied the available interlayer sites for N_2 in the same way as for Fe cations. This strong SSA reduction showed that most nitrogen adsorption sites were between the clay layers.

When INP was produced on the CNa^+ clays, the measured SSA (41.34 g/m^2) was lower than the calculated one of individual components (45.31 g/m^2). This result suggested that rather than being only juxtaposed to clays, a significant percentage of INPs were located between the clay layers, contributing to the decrease of SSA by occupying nitrogen absorption sites. On the contrary, when INP was produced on the C20A clays, the measured SSA (16.06 g/m^2) was slightly higher than the calculated one (13.02 g/m^2).

In the case of C20A, the SSA increase from 9.33 to 16.06 g/m^2 showed that some of Fe cations adsorbed to somewhere other than available surfaces for N_2, like solvent-modified edges and created new adsorption sites. In the modifying process of clays, the intensity of both O−H stretching and H−O−H bending modes strongly decreased and showed that organic modifications decreased the hydrophilic character of the material surface, which could be due to ionic bond of the OH^- groups with ammonium ions.[69] The presence of solvents in the Fe growth step replaced these groups and resulted in adsorbing more Fe cations on these sites.

Cryogenic Mossbauer spectroscopy of Fe^{3+}/Fe^{2+} MMT samples were used to investigate the adsorption preference of each Fe ion on CNa^+ or C20A. The related spectra of Fe^{3+}/Fe^{2+} MMT samples are illustrated in Figure 6.

With reference to Mossbauer spectroscopy results, isomer shift (IS), quadrupole splitting (QS), and reflection width (LW) for Fe^{3+} and Fe^{2+} as the main species in each reflection are summarized in Table 4.

The observation that Fe^{3+} was found in the Fe^{2+}-exchanged samples was in agreement with the work of ref 70, where it was reported that it was too hard to prepare Fe-exchanged MMT without partial oxidation. The parameters of the Fe^{2+} species were similar to those from the hydrated Fe^{2+} ion.[71,72] The Fe^{2+} ions would, therefore, be separated from the clay surfaces by water molecules (mainly in interlayer space of dried clays) which were immobilized in the frozen state.

For Fe02−CNa^+, an additional component was observed (Figure 6d). By analogy with the Fe^{2+} results, this additional component probably occurred from a solvated ion.

For Fe^{3+}, by changing the clay from C20A to CNa^+, there was no significant change in Mossbauer parameters. In this respect, there could be two possibilities. The first possibility was that Fe^{3+} may be directly bound to the silicate structure. The second one was that hydroxy Fe^{3+} polymers may be formed, as similar parameters had been reported for the various oxyhydroxides.[73] If species were surrounded by other molecules like water in cryogenic states, freezing of the surrounding part would change the Mossbauer spectra. Usually, the unchanged state of the

https://doi.org/10.1021/acsomega.2c00286
ACS Omega 2022, 7, 16391−16401

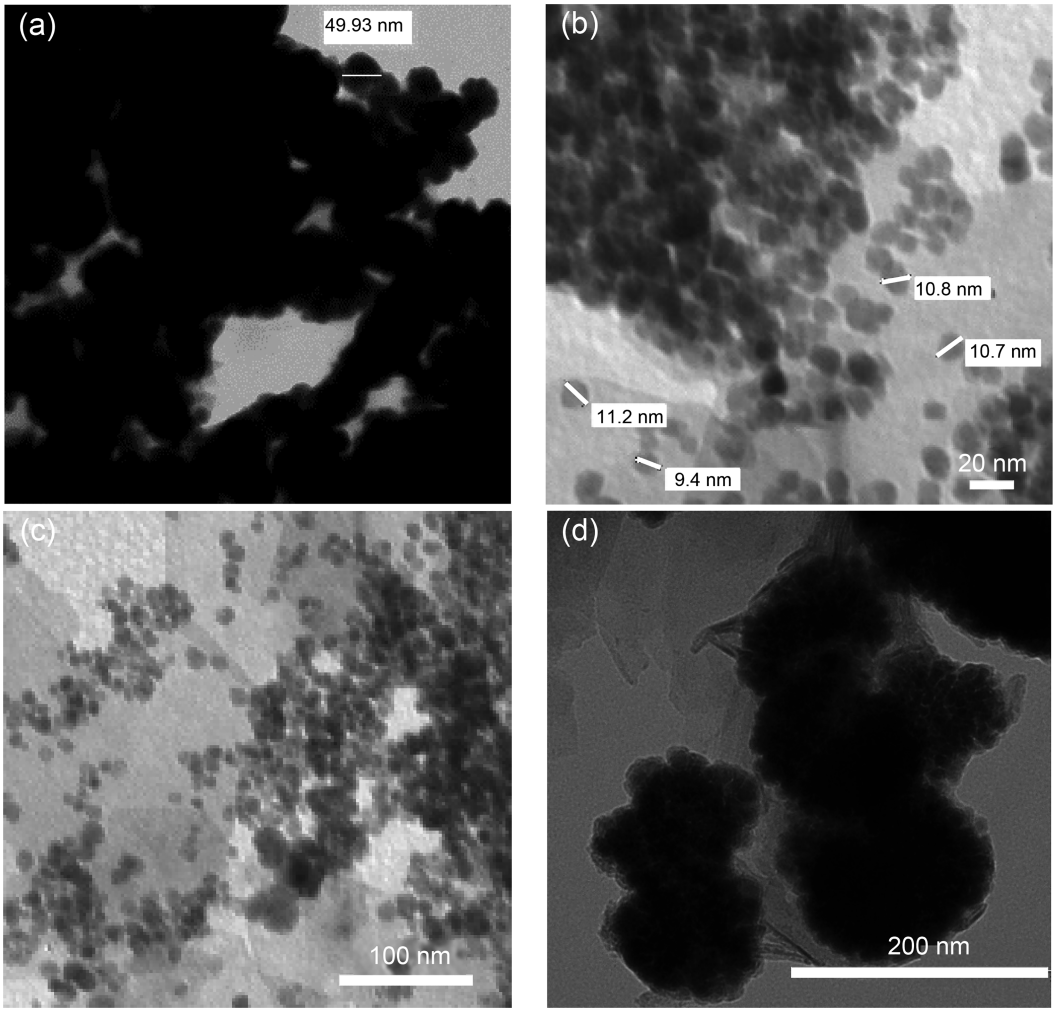

Figure 4. TEM images of (a) Fe03 ZVINP produced alone, (b,c) Fe03−C20A in the presence of selected solvent, and (d) Fe03−C20A after freeze-drying.

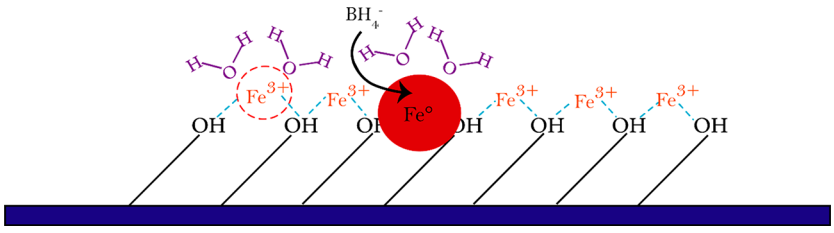

Figure 5. Schematic view of the clay surface effect on Fe cation reduction.

Table 3. Specific Surface Area from N_2 BET Isotherms of Dried Powders (INP/MMT 1:6 w/w)

Parameter	Fe03 ZVINP	CNa^+	Fe03-CNa^+	C20A	Fe03−C20A
measured SSA (g/m^2)	35.17	47.00	41.34	9.33	16.06
calculated SSA (g/m^2)			45.31		13.02

Table 4. Mossbauer Parameters of Main Species in Produced Samples

sample	component	IS (mm/s)	QS (mm/s)	LW (mm/s)	area (%)
Fe03−C20A	Fe^{3+}	0.350	0.753	0.535	84
	Fe^{2+}	1.220	2.270	0.530	16
Fe02−C20A	Fe^{3+}	0.332	0.790	0.566	60
	Fe^{2+}	1.210	2.260	0.490	18
Fe03−CNa^+	Fe^{3+}	0.343	0.766	0.556	55
	Fe^{2+}	1.200	2.240	0.520	11
Fe02−CNa^+	Fe^{3+}	0.305	0.820	0.555	53
	Fe^{2+}	1.221	2.314	0.490	24

spectra was evidence of direct connection of species to the main structure or forming a polymer.

Figure 7 shows the changing of the intercalation and exfoliation extent in CNa^+ and C20A by the INP growth from different cations between platelets. The INP produced from Fe^{2+} cations in C20A and CNa^+ shifted and damped the (001)

https://doi.org/10.1021/acsomega.2c00286
ACS Omega 2022, 7, 16391−16401

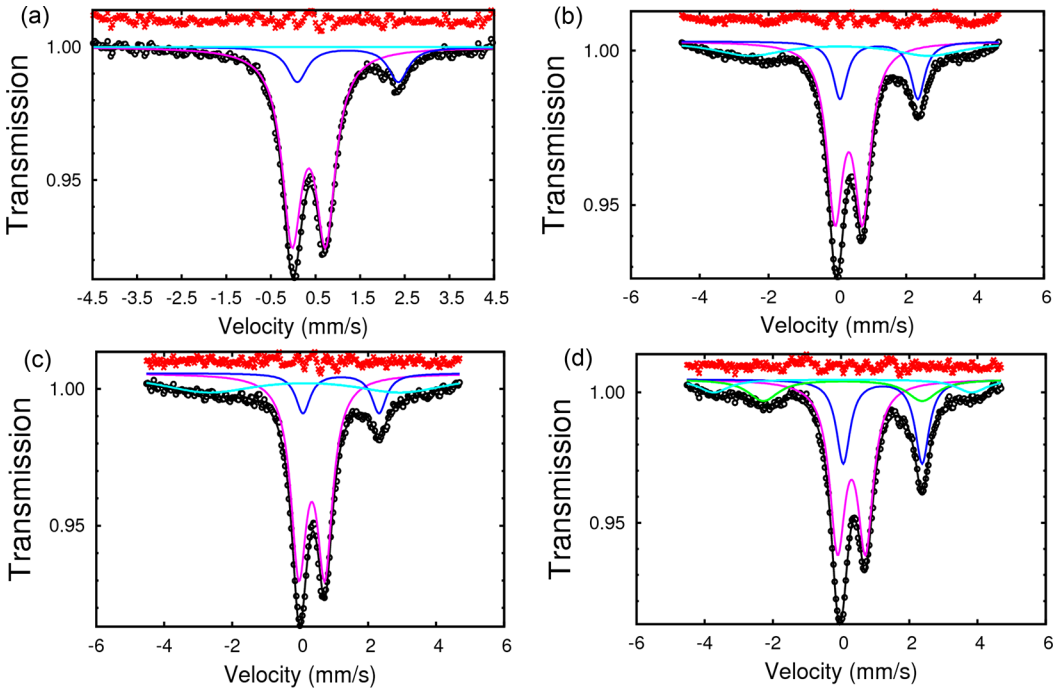

Figure 6. Cryogenic Mossbauer spectra: (a) Fe03−C20A, (b) Fe02−C20A, (c) Fe03−CNa^+, and (d) Fe02−CNa^+. Black dots, experimental data; red dots, misfit = experimental data − fitted data; dark blue line, Fe para; light blue line, Fe magn; green line, solvated ion.

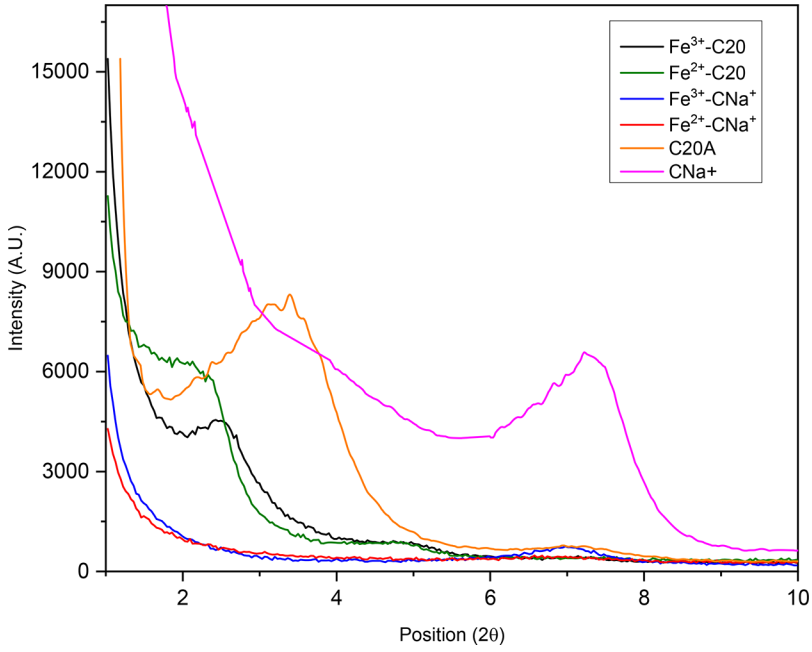

Figure 7. Changing the extent of intercalation and exfoliation in CNa^+ and C20A by INP growth from different cations between clay platelets.

reflection, respectively, which could originate from the main position of this species in the interlayer and also the bigger size. This was in good agreement with the result obtained from Mossbauer spectroscopy. Growing INPs with a few nanometers size from picometer-sized cations pushed the layers out and resulted in intercalation−exfoliation.

3.5. Oxygen Access to Hybrid Nanostructure. Table 5 represents the color changing process in samples over time by absorbing the ambient oxygen as a qualitative criterion. The colors were obtained by the coordinates in a uniform color space consisting of lightness variable, L^*, and chromaticity indices, a^* and b^*. There were some facts which could be concluded from this table. First, the color change in ZVINPs was sharp, whereas it was gradual in INP−clays, which could be due to the retarding effect of the clay. Second, the oxygen absorption was faster and sharper in Fe^{3+}-based INP samples than that in Fe^{2+}-based ones, showing that most Fe^{2+}-based INPs were embedded between the clay platelets and were not available for the oxygen attack. Third, the oxygen absorption in Fe^{3+}-based samples was more gradual with a lag time shorter than that of the Fe^{2+}-based samples, showing the more surface area in these samples due to the dispersing effect of clay sheets and retarded particle

https://doi.org/10.1021/acsomega.2c00286
ACS Omega 2022, 7, 16391−16401

Table 5. Color Changing Process in Samples over Time by Absorbing the Ambient Oxygen

Time/Sample	Fe03-C20A	Fe02-C20A	Fe03-CNa$^+$	Fe02-CNa$^+$	Fe03 ZVINP
Start	CIE-L*ab 39.600 L* -0.640 a* 5.470 b*	CIE-L*ab 31.360 L* -0.480 a* 2.350 b*	CIE-L*ab 34.380 L* -0.100 a* 5.900 b*	CIE-L*ab 30.510 L* -0.220 a* 1.400 b*	CIE-L*ab 25.330 L* 0.160 a* -0.270 b*
1 h	CIE-L*ab 42.840 L* -0.830 a* 8.480 b*	CIE-L*ab 33.130 L* -0.910 a* 3.510 b*	CIE-L*ab 43.740 L* 1.500 a* 16.990 b*	CIE-L*ab 30.740 L* -0.340 a* 2.630 b*	CIE-L*ab 25.550 L* 0.090 a* 0.030 b*
3 h	CIE-L*ab 48.620 L* 0.650 a* 15.960 b*	CIE-L*ab 35.020 L* -0.910 a* 5.790 b*	CIE-L*ab 47.810 L* 5.230 a* 23.870 b*	CIE-L*ab 33.800 L* 0.100 a* 5.130 b*	CIE-L*ab 29.410 L* -0.140 a* 2.400 b*
5 h	CIE-L*ab 51.970 L* 2.810 a* 21.300 b*	CIE-L*ab 36.520 L* -0.440 a* 8.260 b*	CIE-L*ab 48.470 L* 6.300 a* 25.510 b*	CIE-L*ab 34.350 L* 0.720 a* 7.130 b*	CIE-L*ab 32.410 L* -0.010 a* 5.150 b*
1 day	CIE-L*ab 52.380 L* 5.420 a* 25.670 b*	CIE-L*ab 41.600 L* 2.910 a* 17.480 b*	CIE-L*ab 48.160 L* 8.030 a* 28.770 b*	CIE-L*ab 34.170 L* 1.650 a* 9.190 b*	CIE-L*ab 41.770 L* 8.290 a* 24.400 b*
2 days	CIE-L*ab 52.140 L* 6.160 a* 26.960 b*	CIE-L*ab 43.050 L* 4.120 a* 20.080 b*	CIE-L*ab 47.650 L* 8.540 a* 29.540 b*	CIE-L*ab 33.540 L* 1.880 a* 9.580 b*	CIE-L*ab 41.380 L* 11.200 a* 27.100 b*
3 days	CIE-L*ab 51.480 L* 6.790 a* 27.540 b*	CIE-L*ab 43.820 L* 5.000 a* 21.710 b*	CIE-L*ab 46.940 L* 8.850 a* 29.910 b*	CIE-L*ab 33.710 L* 2.250 a* 10.160 b*	CIE-L*ab 40.110 L* 11.930 a* 26.150 b*
4 days	CIE-L*ab 51.550 L* 6.920 a* 27.800 b*	CIE-L*ab 43.900 L* 5.520 a* 22.420 b*	CIE-L*ab 46.830 L* 9.000 a* 30.000 b*	CIE-L*ab 34.160 L* 2.650 a* 11.440 b*	CIE-L*ab 39.780 L* 12.100 a* 25.900 b*
6 days	CIE-L*ab 50.880 L* 7.380 a* 28.550 b*	CIE-L*ab 44.060 L* 6.200 a* 23.480 b*	CIE-L*ab 45.900 L* 9.360 a* 30.140 b*	CIE-L*ab 34.570 L* 3.860 a* 14.270 b*	CIE-L*ab 39.380 L* 12.210 a* 25.960 b*
16 days	CIE-L*ab 51.740 L* 6.730 a* 25.670 b*	CIE-L*ab 44.620 L* 8.610 a* 24.020 b*	CIE-L*ab 40.980 L* 8.550 a* 23.170 b*		

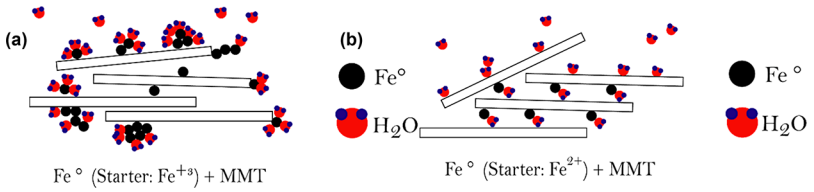

Figure 8. Localization of different iron nanoparticles on montmorillonite clay hosts for oxygen scavenging: (a) Fe0-MMT with Fe^{3+} starter and (b) Fe0-MMT with Fe^{2+} starter.

agglomeration. Fourth, CNa$^+$ clays protected Fe^{2+} INPs longer and Fe^{3+} INPs shorter than C20A clays. So the Fe03-CNa$^+$ hybrid structure could be a choice for fast oxygen scavenging, while Fe02-CNa$^+$ is the better fit for long lasting scavenging.

https://doi.org/10.1021/acsomega.2c00286
ACS Omega 2022, 7, 16391−16401

Based on the information above, localization of different cation-based iron nanoparticles on montmorillonite clays host can be shown as Figure 8. The Fe^{2+} cations tend to embed between clay layers and reduce to Fe^0 INP (Figure 8a) more easily compared to Fe^{3+} cations, which are solvated and bonded to the surface of clay sheets (Figure 8b). Fe^0 generation at the clay interlayer could lead to more intercalation.

4. CONCLUSIONS

In this work, size and localization of iron nanoparticles in the presence of natural or modified montmorillonite clays were studied. The results indicated that reducing Fe cations in the presence of montmorillonite, on one hand, limited the particles, and agglomeration resulting in producing dispersed particles, on the other hand, led to the higher clay intercalation−exfoliation. By changing the cation type of iron particles before reduction and growth, the absorption site on the clay, oxygen scavenging properties of the produced particles, and intercalation−exfoliation state were changed since the Fe^{2+} cations preferred to migrate to the interlayer space while Fe^{3+} tended to bond to the clay surface. Meanwhile, the rate of scavenging in Fe^{3+}-based montmorillonite was more due to availability of iron nanoparticles. Due to the embedding of nanoparticles through the interlayer space, Fe^{2+}-based montmorillonite had more shelf life and its migration probability in the polymer was less than that of embedded Fe^{3+}.

AUTHOR INFORMATION

Corresponding Author

Khadijeh Khederlou − *Institute for Nanoscience and Nanotechnology, Sharif University of Technology, Tehran 13537-13331, Iran;* orcid.org/0000-0001-7832-4820; Email: khadijeh.khederlou@gmail.com

Authors

Reza Bagheri − *Department of Materials Science and Engineering, Sharif University of Technology, Tehran 13537-13331, Iran;* orcid.org/0000-0003-1868-401X

Akbar Shojaei − *Department of Chemical and Petroleum Engineering, Sharif University of Technology, Tehran 13537-13331, Iran;* orcid.org/0000-0003-3708-4706

Nathalie Gontard − *UMR "Ingénierie des Agropolymères et Technologies Emergentes", INRA, Univ. Montpellier, Montpellier SupAgro, CIRAD, Montpellier 34060, France*

Yousef Tamsilian − *Department of Chemical Engineering, Faculty of Engineering, Shahid Chamran University of Ahvaz, Ahvaz 61357-83151, Iran;* orcid.org/0000-0001-6883-910X

Complete contact information is available at: https://pubs.acs.org/10.1021/acsomega.2c00286

Notes

The authors declare no competing financial interest.

ACKNOWLEDGMENTS

The authors are grateful to Dr. Jerome Lacomte in CIRAD, INRA, Montpellier, France, for his kind support and encouragement in this research.

REFERENCES

(1) Diao, M.; Yao, M. Use of zero-valent iron nanoparticles in inactivating microbes. *Water Res.* **2009**, *43*, 5243−5251.

(2) Qu, Zh; Garfinkel, A.; Weiss, J. N.; Nivala, M. Multi-scale modeling in biology: how to bridge the gaps between scales? *Prog. Biophys. Mol.* **2011**, *107*, 21−31.

(3) Fu, F.; Dionysiou, D. D.; Liu, H. The use of zero-valent iron for groundwater remediation and wastewater treatment: areview. *J. Hazard. Mater.* **2014**, *267*, 194−205.

(4) Kumar, N.; Auffan, M.; Gattacceca, J.; Rose, J.; Olivi, L.; Borschneck, D.; Kvapil, P.; Jublot, M.; Kaifas, D.; Malleret, L.; Doumenq, P.; Bottero, J.-Y. Molecular insights of oxidation process of iron nanoparticles: spectroscopic, magnetic, and microscopic evidence. *Environ. Sci. Technol. E* **2014**, *48*, 13888−13894.

(5) Zhao, G.; Wang, J.; Li, Y.; Chen, X.; Liu, Y. Enzymes immobilized on superparamagnetic Fe_3O_4@clays nanocomposites: preparation, characterization, and a new strategy for the regeneration of supports. *J. Phys. Chem. C* **2011**, *115*, 6350−6359.

(6) Yang, Sh; Wu, P.; Liu, J.; Chen, M.; Ahmed, Z.; Zhu, N. Efficient removal of bisphenol a by superoxide radical and singlet oxygen generated from peroxymonosulfate activated with Fe0-montmorillonite. *Chem. Eng. J.* **2018**, *350*, 484−495.

(7) Gil-Diaz, M.; Alvarez, M. A.; Alonso, J.; Lobo, M. C. Effectiveness of nanoscale zero-valent iron for the immobilization of Cu and/or Ni in water and soil samples. *Sci. Rep.* **2020**, *10*, 15927.

(8) Deng, J.; Cheng, Y.; Liu, M.; Tu, B.; Xue, Sh; Tao, H. Fe-Mn Co-embed carbon spheres for aqueous divalent Cd removal. *Colloids Surf. A: Physicochem. Eng. Asp.* **2021**, *612*, 126013.

(9) Wernke, G.; Fernandes Silva, M.; Silva, E. A. d.; Fagundes-Klen, M. R.; Suzaki, P. Y. R.; Triques, C. C.; Bergamasco, R. Ag and CuOnanoparticles decorated on graphene oxide/activated carbon as a novel adsorbent for the removal of cephalexin from fater. *Colloids Surf. A: Physicochem. Eng. Asp.* **2021**, *627*, 127203.

(10) Bao, Sh; Tu, M.; Huang, H.; Wang, C.; Chen, Y.; Sun, B.; Xu, B. Heterogeneous iron oxide nanoparticles anchored on carbon nanotubes for high-performance lithium-ion storage and fenton-like oxidation. *J. Colloid Interface Sci.* **2021**, *601*, 283−293.

(11) Fazio, E.; Santoro, M.; Lentini, G.; Franco, D.; Guglielmino, S. P. P.; Neri, F. Iron oxide nanoparticles prepared by laser ablation: synthesis, structural properties and antimicrobial activity. *Colloids Surf. A: Physicochem. Eng. Asp.* **2016**, *490*, 98−103.

(12) Mohammed, L.; Gomaa, H. G.; Ragab, D.; Zhu, J. Magnetic nanoparticles for environmental and biomedical applications: areview. *Particuology* **2017**, *30*, 1−14.

(13) Meena, J.; Gupta, A.; Ahuja, R.; Singh, M.; Panda, A. K. Recent advances in nano-engineered approaches used for enzyme immobilization with enhanced activity. *J. Mol. Liq.* **2021**, *338*, 116602.

(14) Mu, H.; Gao, H.; Chen, H.; Tao, F.; Fang, X.; Ge, L. A nanosised oxygen scavenger: preparation and antioxidant application to roasted sunflower seeds and walnuts. *Food Chem.* **2013**, *136*, 245−250.

(15) Nathalie, G.; Peyron, S.; Lagaron, J. M.; Echegoyen, Y.; Guillaume, C. Nanotechnologies for active and intelligent food packaging: opportunities and risks. *Nanotechnology in Agriculture and Food Science*; Wiley-VCH: Weinheim, Germany, 2017; pp 177−196.

(16) Macdonald, J. E.; Kelly, J. A.; Veinot, J. G. C. Iron/iron oxide nanoparticle sequestration of catalytic metal impurities from aqueous media and organic reaction products. *Langmuir* **2007**, *23*, 9543−9545.

(17) Karabelli, D.; Uzum, C.; Shahwan, T.; Eroglu, A. E.; Scott, T. B.; Hallam, K. R.; Lieberwirth, I. Batch removal of aqueous Cu^{2+}ions using nanoparticles of zero-valent iron: astudy of the capacity and mechanism of uptake. *Ind. Eng. Chem. Res.* **2008**, *47*, 4758−4764.

(18) Blowes, D. W.; Ptacek, C. J.; Benner, Sh.G.; McRae, Ch.W.T.; Bennett, T. A.; Puls, R. W. Treatment of inorganic contaminants using permeable reactive barriers. *J. Contam. Hydrol.* **2000**, *45*, 123−137.

(19) Zhang, W. Nanoscale iron particles for environmental remediation: an overview. *J. Nanopart. Res.* **2003**, *5*, 323−332.

(20) Panturu, R. L.; Jinescu, G.; Panturu, E.; Filcenco-Olteanu, A.; Radulescu, R. Synthesis and characterization of zero valent iron intended to be used for decontamination of radioactive water. *UPB Sci. Bull. B: Chem. Mater. Sci.* **2010**, *72*, 1454−2331.

https://doi.org/10.1021/acsomega.2c00286
ACS Omega 2022, 7, 16391−16401

(21) Mossa Hosseini, S.; Ataie-Ashtiani, B.; Kholghi, M. Nitrate reduction by nano-Fe/Cu particles in packed column. *Desalination* **2011**, *276*, 214−221.
(22) Lee, Ch; Kim, J. Y.; Lee, W.; Nelson, K. L.; Yoon, J.; Sedlak, D. L. Bactericidal effect of zero-valent iron nanoparticles on escherichia coli. *Environ. Sci. Technol.* **2008**, *42*, 4927−4933.
(23) Kumar, N.; Omoregie, E. O.; Rose, J.; Masion, A.; Lloyd, J. R.; Diels, L.; Bastiaens, L. Inhibition of sulfate eeducing bacteria in aquifer sediment by iron nanoparticles. *Water Res.* **2014**, *51*, 64−72.
(24) Tang, P.; Shen, J.; Hu, Zh; Bai, G.; Wang, M.; Peng, B.; Shen, R.; Linghu, W. High-efficient scavenging of U (Vi) by magnetic Fe_3O_4@ gelatin composite. *J. Mol. Liq.* **2016**, *221*, 497−506.
(25) Raja Beryl, J.; Xavier, J. R. Influence of silane unctionalized nanoclay on the barrier, mechanical and hydrophobic properties by clay nanocomposite films in an aggressive chloride medium. *Colloids Surf. A: Physicochem. Eng. Asp.* **2021**, *630*, 127625.
(26) Brito, J.; Hlushko, H.; Abbott, A.; Aliakseyeu, A.; Hlushko, R.; Sukhishvili, S. A. Integrating antioxidant functionality into polymer materials: fundamentals, strategies, and applications. *ACS Appl. Mater. Interfaces* **2021**, *13*, 41372−41395.
(27) Huber, D. L. Synthesis, properties, and applications of iron nanoparticles. *Small* **2005**, *1*, 482−501.
(28) Ponder, Sh.M.; Darab, J. G.; Mallouk, Th.E. Remediation of Cr (Vi) and Pb (Ii) aqueous solutions using supported, nanoscale zero-Valent iron. *Environ. Sci. Technol.* **2000**, *34*, 2564−2569.
(29) Wang, Ch; Zhang, W. Synthesizing nanoscale iron particles for rapid and complete dechlorination of TCE and PCBs. *Environ. Sci. Technol.* **1997**, *31*, 2154−2156.
(30) Yuan, P.; He, H.; Bergaya, F.; Wu, D.; Zhou, Q.; Zhu, J. Synthesis and characterization of delaminated iron-pillared clay with meso−microporous structure. *Microporous Mesoporous Mater.* **2006**, *88*, 8−15.
(31) Chien, A.; Lee, Y.; Lin, K. Crosslinkable poly(vinyl acetate)/clay nanocomposite films cast from soap-free emulsion-polymerized latices. *J. Appl. Polym. Sci.* **2008**, *109*, 355−362.
(32) Khuntia, B. K.; Anwar, M. F.; Alam, T.; Samim, M.; Kumari, M.; Arora, I. Synthesis and characterization of zero-valent iron nano-particles, and the study of their effect against the degradation of Ddt in soil and assessment of their toxicity against Collembola and Ostracods. *ACS Omega* **2019**, *4*, 18502−18509.
(33) Singh, R.; Misra, V. Stabilization of Zero-Valent Iron Nano-particles: Role of Polymers and Surfactants. *Handbook of Nanoparticles*; Springer: Cham, Switzerland, 2015; pp 1−19.
(34) He, F.; Zhao, D. Manipulating the size and dispersibility of zerovalent iron nanoparticles by use of carboxymethyl cellulose stabilizers. *Environ. Sci. Technol.* **2007**, *41*, 6216−6221.
(35) Molina, L.; Gaete, J.; Alfaro, I.; Ide, V.; Valenzuela, F.; Parada, J.; Basualto, C. Synthesis and characterization of magnetite nanoparticles functionalized with organophosphorus compounds and its application as an adsorbent for La (iii), Nd (iii) and Pr (Iii) ions from aqueous solutions. *J. Mol. Liq.* **2019**, *275*, 178−191.
(36) Stoller, M.; Palma, L. D.; Vilardi, G. Soil Remediation by Zero-Valent Iron Nanoparticles for Organic Pollutant Elimination. *Nano-structured Materials for Environmental Applications*; Springer, 2021; pp 247−266.
(37) Qiang, Y.; Antony, J.; Sharma, A.; Nutting, J.; Sikes, D.; Meyer, D. Iron/iron oxide core-shell nanoclusters for biomedical applications. *J. Nanopart. Res.* **2006**, *8*, 489−496.
(38) Lakkaboyana, S. K.; Khantong, S.; Asmel, N. K.; Obaidullah, S.; Kumar, V.; Kannan, K.; Venkateswarlu, K.; Yuzir, A.; Wan Yaacob, W. Z. Indonesian kaolin supported Nzvi (Ik-Nzvi) used for anefficient removal of Pb (ii) from aqueous solutions: kinetics, thermodynamics and mechanism. *J. Environ. Chem. Eng.* **2021**, *9*, 106483.
(39) Wang, H.; Wang, L.; Xiao, F. Metal@zeolite hybrid materials for catalysis. *ACS Cent. Sci.* **2020**, *6*, 1685−1697.
(40) Xingu-Contreras, E.; García-Rosales, G.; Cabral-Prieto, A.; García-Sosa, I. Degradation of methyl orange using iron boride nanoparticles supported in a natural zeolite. *Environ. Nanotechnol. Monit. Manag.* **2017**, *7*, 121−129.
(41) Kim, S. A.; Kamala-Kannan, S.; Lee, K.-J.; Park, Y.-J.; Shea, P. J.; Lee, W.-H.; Kim, H.-M.; Oh, B.-T. Removal of Pb (ii) from aqueous solution by a zeolite−nanoscale zero-valent iron composite. *Chem. Eng. J.* **2013**, *217*, 54−60.
(42) Chen, Zh; Jin, X.; Chen, Z.; Megharaj, M.; Naidu, R. Removal of methyl orange from aqueous solution using bentonite-supported nanoscale zero-valent iron. *J. Colloid Interface Sci.* **2011**, *363*, 601−607.
(43) Zheng, M.; Qiu, D.; Zhao, B.; Ma, L.; Wang, X.; Lin, Z.; Pan, L.; Zheng, Y.; Shi, Y. Mesoporous iron oxide directly anchored on a graphene matrix for lithium-ion battery anodes with enhanced strain accommodation. *RSC Adv.* **2013**, *3*, 699−703.
(44) Kamat, P. V. Graphene-based nanoarchitectures. anchoring semiconductor and metal nanoparticles on a two-dimensional carbon support. *J. Phys. Chem. Lett.* **2010**, *1*, 520−527.
(45) Fan, M.; Yuan, P.; Zhu, J.; Chen, T.; Yuan, A.; He, H.; Chen, K.; Liu, D. Core−shell structured iron nanoparticles well dispersed on montmorillonite. *J. Magn. Magn. Mater.* **2009**, *321*, 3515−3519.
(46) Bhowmick, S.; Chakraborty, S.; Mondal, P.; Van Renterghem, W.; Van den Berghe, S.; Roman-Ross, G.; Chatterjee, D.; Iglesias, M. Montmorillonite-supported nanoscale zero-valent iron for removal of arsenic from aqueous solution: kinetics and mechanism. *Chem. Eng. J.* **2014**, *243*, 14−23.
(47) Shahwan, T.; Uzum, C.; Eroglu, A.E.; Lieberwirth, I. Synthesis and characterization of bentonite/iron nanoparticles and their application as adsorbent of cobalt ions. *Appl. Clay Sci.* **2010**, *47*, 257−262.
(48) Uzum, C.; Shahwan, T.; Eroglu, A. E.; Hallam, K. R.; Scott, Th.B.; Lieberwirth, I. Synthesis and characterization of kaolinite-supported zero-valent iron nanoparticles and their application for the removal of aqueous Cu^{2+} and Co^{2+}ions. *Appl. Clay Sci.* **2009**, *43*, 172−181.
(49) Zhao, Q.; Fu, L.; Jiang, D.; Ouyang, J.; Hu, Y.; Yang, H.; Xi, Y. Nanoclay-modulated oxygen vacancies of metal oxide. *Commun. Chem.* **2019**, *2*, 11.
(50) Hossain, M. F.; Paul, T. C.; Khan, M. N. I.; Islam, S.; Bala, P. Magnetic and dielectric properties of $ZnFe_2O_4$/nanoclay composites synthesized via sol-gel autocombustion. *Mater. Chem. Phys.* **2021**, *271*, 124914.
(51) Zhai, Sh; Zheng, Q.; Ge, M. Nanosized mesoporous iron Manganese bimetal oxides anchored on natural kaolinite as highly efficient hydrogen peroxide catalyst for polyvinyl alcohol degradation. *J. Mol. Liq.* **2021**, *337*, 116611.
(52) Mohan, D.; Pittman, Ch.U.J. Arsenic removal from water/wastewater using adsorbents—a critical review. *J. Hazard. Mater.* **2007**, *142*, 1−53.
(53) Sohrabi, N.; Mohammadi, R.; Ghassemzadeh, H. R.; Heris, S. S. S. Equilibrium, kinetic and thermodynamic study of diazinon adsorption from water by clay/Go/Fe_3O_4: modeling and optimization based on response surface methodology and artificial neural network. *J. Mol. Liq.* **2021**, *328*, 115384.
(54) Letaïef, S.; Aranda, P.; Ruiz-Hitzky, E. Influence of iron in the formation of conductive polypyrrole-clay nanocomposites. *Appl. Clay Sci.* **2005**, *28*, 183−198.
(55) Oliveira, L. C.A; Rios, R. V.R.A; Fabris, J. D; Sapag, K.; Garg, V. K; Lago, R. M Clay−iron oxide magnetic composites for the adsorption of contaminants in water. *Appl. Clay Sci.* **2003**, *22*, 169−177.
(56) Basegio, T. M.; Garcia, A. P.; Bergmann, C. P. Nanostructured Zero-Valent Iron: From Synthesis to Application. In *Environmental Applications of Nanomaterials. Engineering Materials*; Kopp Alves, A., Ed.; Springer: Cham, Switzerland, 2022.
(57) Utracki, L. A. *Clay-Containing Polymeric Nanocomposites*; iSmithers Rapra Publishing, 2004.
(58) Busolo, M. A.; Lagaron, J. M. Oxygen scavenging polyolefin nanocomposite films containing an iron modified kaolinite of interest in active food packaging applications. *Innov Food Sci. Emerg Technol.* **2012**, *16*, 211−117.
(59) Bergaya, F.; Lagaly, G. *Handbook of Clay Science*; Newnes, 2013.
(60) Alexander, L.; Klug, H. P. Determination of crystallite size with the X-ray spectrometer. *J. Appl. Phys.* **1950**, *21*, 137−142.

https://doi.org/10.1021/acsomega.2c00286
ACS Omega 2022, 7, 16391−16401

(61) Shchukarev, S. A.; Tolmacheva, T. A. Solubility of oxygen in ethanol-water mixtures. *J. Struct. Chem.* **1968**, *9*, 16−21.
(62) Sun, X.; Fang, J. M.; Xu, R.; Wang, M.; Yang, H.; Han, Zh; Xu, J. Nanoscale zero-valent iron immobilized inside the mesopores of ordered mesoporous carbon by the "two solvents" reduction technique for Cr (Vi) and as (V) removal from aqueous solution. *J. Mol. Liq.* **2020**, *315*, 113598.
(63) Glavee, G. N.; Klabunde, K. J.; Sorensen, Ch.M.; Hadjipanayis, G. C. Chemistry of borohydride reduction of iron (ii) and iron (iii) ions in aqueous and nonaqueous media. formation of nanoscale Fe, FeB, and Fe_2Bpowders. *Inorg. Chem.* **1995**, *34*, 28−35.
(64) Mohapatra, M.; Anand, S. Synthesis and applications of nano-structured iron oxides/hydroxides−a review. *Int. J. Eng. Sci. Technol.* **2011**, *2*, 2.
(65) Favela-Camacho, S. E.; Samaniego-Benítez, E. J.; Godínez-García, A.; Avilés-Arellano, L. M.; Pérez-Robles, J. F. How to decrease the agglomeration of magnetite nanoparticles and increase their stability using surface properties. *Colloids Surf. A: Physicochem. Eng. Asp.* **2019**, *574*, 29−35.
(66) Yan, H.; Zhang, Z. Effect and mechanism of cation species on the gel properties of montmorillonite. *Colloids Surf. A: Physicochem. Eng. Asp.* **2021**, *611*, 125824.
(67) Lu, X.; Mi, Y. Characterization of the interfacial interaction between polyacrylamide and silicon substrate by fourier transform infrared spectroscopy. *Macromolecules* **2005**, *38*, 839−843.
(68) Kombaya-Touckia-Linin, E.; Gaucel, S.; Sougrati, M. T.; Khederlou, Kh; Pen, N.; Stievano, L.; Gontard, N.; Guillard, V. Hybrid iron montmorillonite nano-particles as an oxygen scavenger. *Chem. Eng. J.* **2019**, *357*, 750−760.
(69) Nguemtchouin, M. G. M.; Ngassoum, M. B.; Kamga, R.; Deabate, S.; Lagerge, S.; Gastaldi, E.; Chalier, P.; Cretin, M. Characterization of inorganic and organic clay modified materials: an approach for adsorption of an insecticidal terpenic compound. *Appl. Clay Sci.* **2015**, *104*, 110−118.
(70) Helsen, J. A.; Goodman, B. A. Characterization of iron (ii)-and Iron (iii)-exchanged montmorillonite and hectorite using the mössbauer effect. *Clay Miner.* **1983**, *18*, 117−125.
(71) Tu, B.; Chen, H.; Xue, Sh; Deng, J.; Tao, H. Ultrafast and efficient removal of aqueous Cr(VI) ising iron oxide nanoparticles supported on bermuda grass-based activated carbon. *J. Mol. Liq.* **2021**, *334*, 116026.
(72) Lakatos, B.; Korecz, L.; Meisel, J. Comparative study on the mössbauer parameters of iron humates and polyuronates. *Geoderma* **1977**, *19*, 149−157.
(73) Goodman, B. A.; Lewis, D. G. Mössbauer spectra of aluminous goethites (α-FeOOH). *J. Soil Sci.* **1981**, *32*, 351−364.

https://doi.org/10.1021/acsomega.2c00286
ACS Omega 2022, 7, 16391−16401